

# Photonic Quantum-Accelerated Machine Learning

Markus Rambach,<sup>1,\*</sup> Abhishek Roy,<sup>1,2</sup> Alexei Gilchrist,<sup>2</sup> Akitada Sakurai,<sup>3</sup>  
William J. Munro,<sup>3</sup> Kae Nemoto,<sup>3</sup> and Andrew G. White<sup>1</sup>

<sup>1</sup>*Quantum Technology Laboratory, School of Mathematics and Physics,  
University of Queensland, Brisbane QLD 4072, Australia*

<sup>2</sup>*Department of Physics and Astronomy, Macquarie University, Sydney NSW 2113, Australia*

<sup>3</sup>*Okinawa Institute of Science and Technology Graduate University, Onna-son, Okinawa 904-0495, Japan*

(Dated: December 10, 2025)

Machine learning is widely applied in modern society, but has yet to capitalise on the unique benefits offered by quantum resources. Boson sampling—a quantum-interference based sampling protocol—is a resource that is classically hard to simulate and can be implemented on current quantum hardware. Here, we present a quantum accelerator for classical machine learning, using boson sampling to provide a high-dimensional quantum fingerprint for reservoir computing. We show robust performance improvements under various conditions: imperfect photon sources down to complete distinguishability; scenarios with severe class imbalances, classifying both handwritten digits and biomedical images; and sparse data, maintaining model accuracy with twenty times less training data. Crucially, we demonstrate the acceleration and scalability of our scheme on a photonic quantum processing unit, providing the first experimental validation that boson-sampling-enhanced learning delivers real performance gains on actual quantum hardware.

Machine learning (ML) and quantum physics are two of the most transformative fields in the modern era of science and technology. ML has made significant advances in the last decade, especially in the last few years, and has firmly entered in the mainstream of every-day life. Quantum is not quite at the same point yet, but it is becoming more prominent to the public and increasingly integrated into emerging technologies, where it promises to advance our capabilities and open new pathways beyond classical limits. This leads to an obvious question: how can these two fields help each other? ML is already used widely to optimise quantum algorithms [1–3] and create or enhance quantum experiments [4–6], however, it has not yet tapped into the potential of real-world improvements that quantum offers in return. Here, we tackle this issue and investigate how quantum resources can augment or accelerate learning in verifiable and relevant ways, laying the groundwork for new quantum-classical hybrid computational models.

Recently, landmark quantum experiments in several physical platforms [7–12] have established computational tasks for which quantum systems outperform their best-known classical simulators. Unfortunately, these demonstrations—often relying on random circuit sampling or related approaches—rarely provide useful outputs outside of showing general advantage and in benchmarking contexts. In other words, while quantum processors can produce distributions inaccessible to classical algorithms within a reasonable time, those distributions are not typically aligned with any practical application.

The best-studied example is *boson sampling*, a task in which  $N$  indistinguishable single photons are injected into an  $M$ -mode interferometer and the output distribution is sampled [13–17]. This task is considered classically intractable and provides a super-

exponential advantage—scaling as  $N^N$  compared to classical computation—but so far this advantage has not been harnessed to advance other domains directly. Building on recent efforts to connect boson sampling with machine learning [18–22], we aim to extend its scope towards more practically relevant tasks.

In classical ML, reservoir computing [23, 24] is a framework where a fixed non-linear dynamical system—the reservoir—projects inputs into a high-dimensional space. Then, only a simple readout layer is trained to extract useful features. A crucial aspect of this framework is that the reservoir is static and not trained. Quantum reservoir computing [25–29]—and its variants, quantum extreme learning machine [30, 31], and quantum extreme reservoir computing [32, 33]—extend reservoir computing to quantum systems, exploiting their naturally rich, high-dimensional and non-linear dynamics. Boson sampling can act as an intrinsically complex reservoir, creating a high-dimensional *fingerprint* of the data. This can then be used as additional inputs by a classifier, e.g., for categorising images [19–21, 34, 35], a crucial task in autonomous driving and medical diagnostics.

A recent proposal, Quantum Optical Reservoir Computing (QORC) [18], introduces a quantum reservoir to accelerate the performance of a linear classifier, achieving higher accuracies while retaining the same training constraint—only the single readout layer is trained. This can be efficiently implemented on a quantum processing unit (QPU) consisting of an integrated photonic chip, Fock-state inputs, and single-photon bucket detectors without the need for number-resolving capabilities. In practice, we see quantum acceleration through lower requirements on the size of the training dataset and the number of training epochs in all investigated scenarios. QORC also outperforms small shallow neural networks in

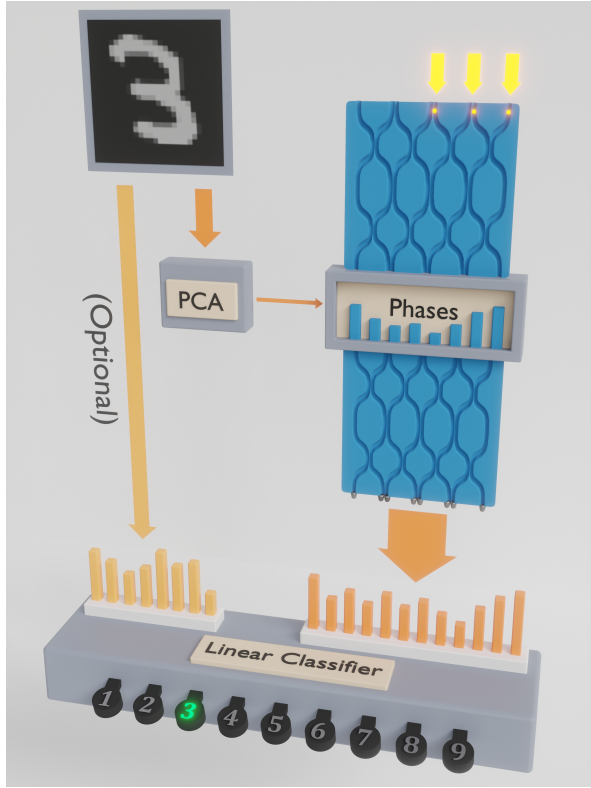


FIG. 1. Quantum Optical Reservoir Computing scheme. An input image (top left) from a set of potential datasets is initially processed: 1) principal component analysis (PCA, right arrow), and 2) optional linearisation from 2D to 1D (left arrow). The first  $M$  components—matching the number of utilised modes—are forwarded to the boson sampling setup (thin arrow). The setup consists of photons entering a pre-circuit (top right), then a layer where the PCA phases are encoded (centre), and finally the reservoir (bottom right). The processed data is the input to the linear classifier (bottom), which finally finds the predicted classification label.

terms of accuracy, while incorporating the reservoir into such network architectures leads to further performance gain.

Fig. 1 illustrates the workflow of QORC. We process data—in our case images—by first applying dimensionality reduction techniques to extract key features and map them onto phases in the quantum circuit. These phases can be imprinted on multi-photon quantum states—photon number  $N$ —via a set of phase shifters between two random interferometer circuits—*pre-circuit* and *reservoir*—of a photonic integrated chip. The two random interferometers can differ, although for simplicity we have chosen them to be the same in all our experiments.

We measure the multi-mode output—mode number  $M$ —through single photon detection without number-resolving capabilities, to obtain a high-dimensional distribution of multi-photon coincidences. This is standardised and, if required, combined with the original classical features before being passed to the linear classifier.

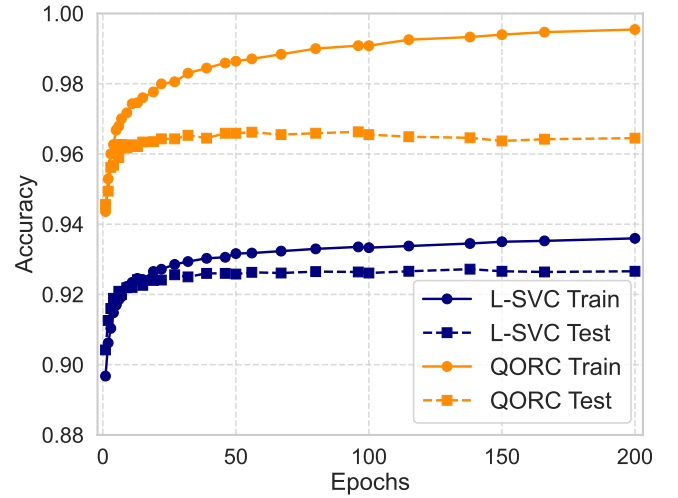


FIG. 2. MNIST classification accuracy as a function of training epochs. QORC in orange, L-SVC in blue. Training (circles, solid lines) on 60000 images, testing (squares, dashed lines) on 10000 images. For each image, the reservoir is 30000 samples. QORC outperforms the best value of L-SVC from the very first training epoch. Data points are connected for better visibility. Best performance on both models is between 50-100 epochs.

Unlike typical quantum models requiring optimisation or back propagation, QORC relies on random, fixed interferometers and uses the quantum evolution to non-linearly expand the feature space, enabling improved performance on non-linear classification tasks [18].

To evaluate the computational potential of QORC, we examine its ability to accelerate image classification tasks across a range of configurations. We investigate two inherently balanced datasets: in the main paper the MNIST dataset [36], 70000 handwritten digits as 28-by-28 pixel greyscale images; and in the Supplementary Material Sec. [S1], the smaller DIGITS data set [37], 1797 images of 8-by-8 handwritten digits.

Biomedical diagnostics represent an important challenge to ML due to their often largely class-imbalance datasets which occur frequently in real-world applications. Such datasets—with one dominant class and significantly fewer images of other diagnostically more relevant classes—stress test many models as they tend to be biased towards majority classes, and underperform on rare but clinically critical cases [38]. Accordingly, we explore the performance on MedMNISTv2 [39], a variety of biomedical image datasets in greyscale and colour, all standardised to 28-by-28 pixels as well.

We numerically investigate a range of configurations, one to five photons,  $N=1-5$ , into  $M=12/20/24$  optical modes; experimentally, we use  $N=3$  and  $M=12$ . This is informed by various factors: 1) the available QPUs on the Quandela cloud architecture, which offer either 12 (Ascella) or 24 (Belenos) modes; 2) reasonable runtimes for the necessary number of samples on the QPU and

hence a combination of the photon number and internal losses in the cloud system; 3) already available numerical simulations from our prior work [18]; 4) reasonable runtimes on the local numerical simulations; and 5) fulfilling the boson sampling condition of ideally keeping  $M > N^2$ . All simulations assume noiseless operation, i.e., they are performed with ideal sources—perfect multi-photon suppression  $g^{(2)}=0$ , and ideal quantum indistinguishability  $\mathcal{I}=0$ —and lossless QPUs, unless stated otherwise.

We consider a simple and lightweight linear support vector classifier (L-SVC) based on the single-perceptron model with multiple output classes [40] for most of our investigations. The model is built in Keras, a high-level neural network interface based on TensorFlow for computation. It is constructed as a linear sequence of an input layer of variable size—dependent on whether a reservoir is used and its size—and an output layer for the possible outcomes/classes. The model is then optimised using the AdaGrad algorithm with a learning rate  $\eta=0.05$ , a batch size of 128, and 100 epochs, unless stated otherwise.

Fig. 2 shows the performance of QORC on MNIST classification as a function of the number of training epochs for a simulated quantum reservoir with  $N=3$  and  $M=20$ . It highlights the performance improvements of the QORC (orange) over the non-accelerated classification (blue). In both cases, the training accuracy (circles, solid lines) is above the test accuracy (squares, dashed lines) as expected. The test accuracies stagnate after around 50 epochs, and get lower for higher num-

Input Data	Accuracy (%)			
	Train	Test	$\Delta$ L-SVC	RPE
<i>N = 3, M = 20</i>				
i) Original data	93.4	92.6	—	0.295
ii) QORC	99.2	96.6	4.0	0.365
iii) Reservoir only	98.1	95.5	2.9	0.365
iv) Original + PCA	93.3	92.6	0.0	0.295
<i>N = 5, M = 24</i>				
i) Original data	93.6	92.7	—	0.295
ii) QORC	100.0	97.6	4.9	3.230
iii) Reservoir only	100.0	97.6	4.9	3.120
iv) Original + PCA	93.5	92.7	0.0	0.295

TABLE I. MNIST linear classification (L-SVC) results for different input data: i) original input data; ii) our scheme (QORC); iii) using the reservoir only; and iv) adding the PCA to the original data. Training on 60000 images for 100 epochs, testing on 10000 images. *top*: 3 photons into 20 modes (1,140 additional inputs). *bottom*: 5 photons into 24 modes (42,504 additional inputs).  $\Delta$ L-SVC is the difference from the input of the original data only. RPE is the runtime per epoch in seconds on a single Apple M2 Max chip. The increase is related to training additional weights of the network,  $>2\times$  and  $>50\times$  for the smaller and larger reservoir, respectively.

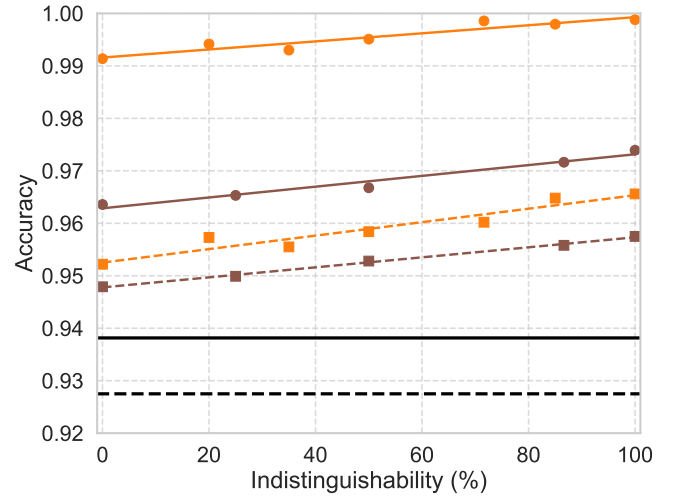


FIG. 3. MNIST classification accuracy as a function of single photon indistinguishability. QORC with  $N=3, M=12$  in brown,  $N=3, M=20$  in orange, and L-SVC included in black as reference. Training (circles, solid lines) on 60000 images for 100 epochs, testing (squares, dashed lines) on 10000 images. For each image, the reservoir is 30000 samples. Coloured fitted lines to guide the eye only. All accuracies for all indistinguishabilities of either reservoir size here surpass the maximal achievable training accuracy of L-SVC.

ber of epochs in the QORC case as a result of overfitting of the training data due to the largely increased input space. We observe this overfitting in various scenarios under investigation, hence we will state all accuracies for 100 epochs from here on. (See Supplemental Material Sec. [S2] for more details). We can also see that our scheme outperforms the best value of L-SVC from the very first epoch, highlighting the quantum acceleration in the number of required training runs.

We furthermore compare the performance of the classifier under different inputs: i) L-SVC on the original data; ii) original data plus reservoir (QORC); iii) reservoir only [41]; and iv) original data plus PCA. Table I shows the results: for ii) we see an increase in test accuracy of 4.0% if we add the reservoir to the original data for a reservoir of  $N=3, M=20$ , which is 1,140 additional inputs. Using the reservoir only, iii), the advantage shrinks to a still significant 2.9%, and finally, if we add the PCA to the original input, iv), the advantage disappears as expected, as the linear PCA simply gets incorporated in the L-SVC network. Similarly, if we move to  $N=5, M=24$ —an additional 42504 inputs to the network—the advantage jumps to 4.9%. This is independent of whether the original MNIST data is added or not, as the reservoir now incorporates all relevant features for learning. Again, adding the PCA yields no advantage. Further analysis of the effect of the number of photons on the model accuracy for a fixed number of modes  $M=20$  as well as the reproducibility of results for different unitaries and input states can be found in the Supplemental

Material Sections S3 and S4.

The performance of the interferometric circuits—*precircuit* and the *reservoir* [18]—for the boson sampling strongly depends on the quality of the single photon Fock states. We quantify the quality through multi-photon suppression and indistinguishability. The latter plays an especially crucial role, as it effectively tunes the system between regimes dominated by first- and second-order quantum coherence. Completely distinguishable photons exhibit no intensity correlations with one another, yet retain coherence in their field amplitude and can therefore interfere with themselves. In Fig. 3 we fix the multi-photon suppression at the experimentally achieved value,  $g^{(2)}=1.95\%$ , and vary the HOM indistinguishability  $\mathcal{I}$ , for the quantum reservoirs  $N=3$  &  $M=12$  (brown),  $N=3$  &  $M=20$  (orange), and the original data (black). Again, the training accuracies are represented by circles and solid lines while the test accuracies by squares and dashed lines.

We observe that higher indistinguishability is correlated with higher training accuracy: the more entangled the Hilbert space, the higher the dimensionality and the finer the quantum fingerprint. Even for fully distinguishable photons ( $\mathcal{I}=0$ ), QORC remains advantageous due to first-order quantum coherence. While the Hilbert-space dimensionality is reduced compared to the entangled regime ( $\mathcal{I}>0$ ), QORC nonetheless provides additional informational capacity that improves classification. Naturally, the larger quantum reservoir performs better, however, a large improvement over 2% between different reservoirs is only found in the training accuracies, not in testing where the improvement is below 1%.

We now explore QORC performance on data sets with different imbalances. Real-world data is often imbalanced—e.g., in biomedical imaging or fraud

Input Data	Macro F1 Score	
	Train	Test
Balanced (L-SVC)	0.941 (2)	0.914 (2)
Balanced (QORC)	0.9998 (7)	0.949 (2)
Gaussian (L-SVC)	0.993 (4)	0.886 (3)
Gaussian (QORC)	0.9998 (2)	0.931 (3)
Severely Imbalanced (L-SVC)	0.929 (9)	0.846 (12)
Severely Imbalanced (QORC)	0.9999 (1)	0.894 (8)

TABLE II. MNIST classification macro F1 scores for differently balanced datasets, QORC for  $N=3, M=20$ . Values are the mean of 100 different subsets of training data, errors (in brackets) are the standard deviation. Training for 100 epochs with  $\sim 10000$  train images, evaluation on 10000 test images. Top: balanced training data between all categories; Middle: Gaussian filter with  $\mu=4.75, \sigma=2$ ; Bottom: Severely imbalanced training data with  $\sim 2 \times (64.3\%)$  images in majority category compared to the sum of all other categories.

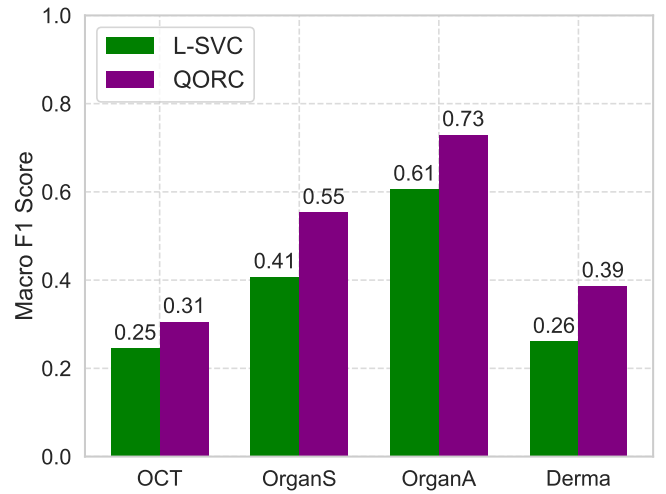


FIG. 4. QORC classification F1 score improvements on different datasets in MedMNISTv2 for 200 training epochs. Quantum reservoir:  $N=3, M=20$ . For each image, the reservoir is 30000 samples. OCT, OrganS, and OrganA are all greyscale images, Derma is in colour. See Supplemental Material Sec. [S5] for more details on the datasets.

detection—where many more samples are available in common classes—healthy people or non-fraudulent transactions—compared to rare but critical ones—diseases or security risks. These two examples show that imbalance is not a mere data collection artifact but rather reflects structural characteristics. Models often achieve good performance in majority classes, but struggle on minority classes, leading to poor classification of cases with larger significance [42]. Here, accuracy as a metric for performance can be misleading, as a naive classifier that simply predicts the favoured majority class can achieve deceptively high accuracies. Hence, we move to a different criterion—the macro F1 score—to assess the performance of our models. The macro F1 score is a simple metric that computes the harmonic mean of precision and recall for each class and then averages across all classes, weighing all components the same and hence taking class imbalance into account. A value close to *one* indicates the model performs well across all classes, a low value close to *zero* hints at poor model performance on one or multiple classes, even if the overall accuracy is still high (see Supplemental Material Sec. [S5] for more details).

We start by artificially creating two imbalanced training datasets of 10000 images derived from MNIST and evaluate the performance of QORC ( $N=3, M=20$ ). The first one applies a Gaussian filter with  $\mu=4.75, \sigma=2$  to the training set, i.e., the number *five* will be the majority (20%) and the number *zero* the smallest class (1.2%). Similarly, the second more severely imbalanced dataset has a majority (minority) class of 64% (0.6%) which are then randomly distributed across the 10 categories for each new training trial (refer to Supplemental Material Sec. [S5] for further details). For a fair comparison, we

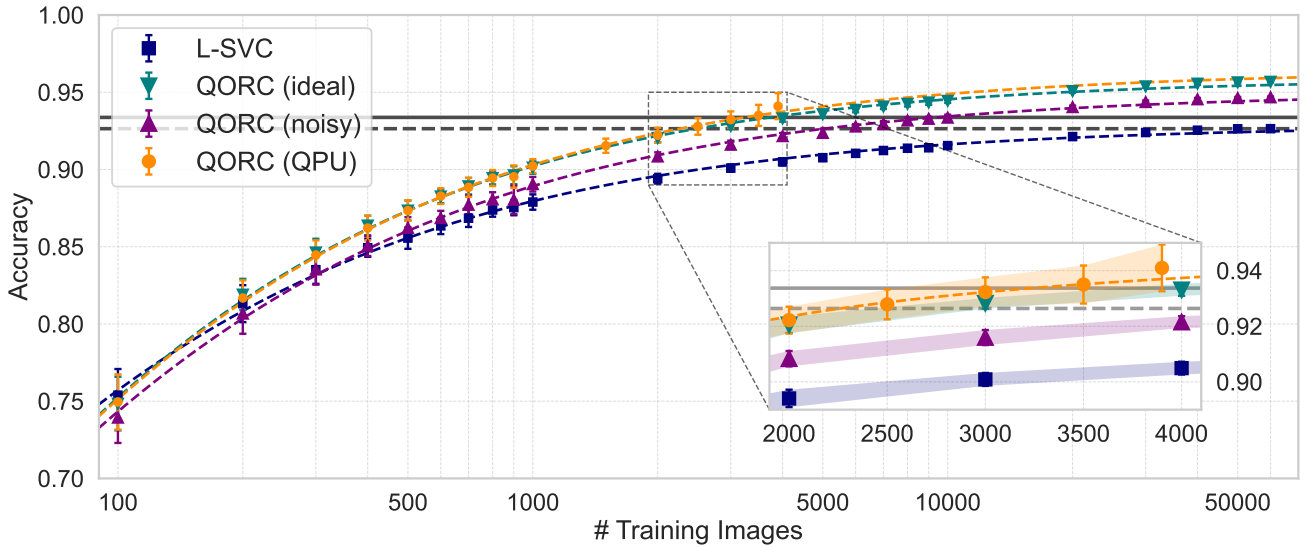


FIG. 5. MNIST classification accuracy dependent on (balanced) training dataset size  $n_{tr}$ . L-SVC in blue squares, QORC with  $N=3, M=12$  in teal triangles (ideal, no noise), purple inverted triangles (noisy,  $g^{(2)}=1.95\%$ ,  $\mathcal{I}=0$ ), and orange circles (QPU,  $g^{(2)}=1.95\%$ ,  $\mathcal{I}=86.36\%$ ). Error bars are the standard deviation on 50 subsets of training data: too small to see for large numbers of training images, but significant for smaller  $n_{tr}$  and the QPU data. Grey lines show the best possible performances for train (solid) and test (dashed) accuracies with L-SVC. Training for 100 epochs, testing (dashed lines) on  $n_{te}=10000$  images apart from QPU data, where  $n_{te} = 4669 - n_{tr}$ . Main: Dashed coloured lines to guide the eye only, Hill function fit:  $L/(1 + (x_{50}/x)^k)$  with  $(L, k, x_{50}) = (0.929, 0.61, 8.6), (0.959, 0.64, 13.3), (0.950, 0.61, 13.2), (0.964, 0.62, 13.1)$  for L-SVC and QORC (ideal, noisy, QPU), respectively. Inset: Shaded regions indicate  $1\sigma$  band. No QPU data available beyond  $n_{tr} = 3900$ .

also reduced the size of the balanced MNIST training data to match. Individual images for training are chosen randomly for each trial to determine the mean F1 and its standard deviation, shown in Table II. We can see that QORC still improves the F1 score for all datasets on both training and test images, demonstrating its significant value for real-world applications.

We also test the algorithm on more meaningful, imbalanced biomedical data from the MedMNISTv2 dataset. This large-scale collection of lightweight biomedical image datasets is specifically designed for benchmarking machine learning algorithms across diverse medical imaging techniques and tasks [39]. The performance of any classifier on MedMNISTv2 is significantly worse compared to standard MNIST as the images are more complex and varied, the signal-to-noise is lower, and generally the classes are not visually obvious and labels might be imperfect. Our results are compared in Fig. 4. Despite the macro F1 scores being significantly lower compared to Table II, QORC still yields improvement in all investigated scenarios.

The significant improvement on both imbalanced and more complex datasets is a very promising sign of QORCs capability to extend robust and generalizable learning to challenging real-world tasks. Our results suggest that QORC can effectively adapt to diverse data distributions and maintain strong performance beyond controlled benchmark settings.

Seeing that QORC exceeds the performance of the L-SVC for any input photon number—see Supplemental

Material Sec. [S4] for details on different  $N$  for  $M=20$ —and all investigated datasets, the crossover point of the performance in terms of training data requirements becomes of interest. It is crucial for ML models to still perform well with limited training data, as data collection is often costly and impractical in real-world scenarios. Additionally, demonstrated robustness can hint at strong generalisation capabilities, with the model capable of learning meaningful patterns rather than noise.

Fig. 5 illustrates the performance differences on random, balanced subsets of training data on MNIST. We can see that QORC surpasses the maximally possible testing accuracy of L-SVC (black dashed) at around 2500 training images for a perfect noiseless single photon source (teal triangles), a significant improvement of  $(23.5^{+0.5}_{-3.5})$  times compared to the 60000 images used to reach peak performance in the L-SVC. In the case of completely distinguishable photons (purple inverted triangles), the advantage shrinks to  $11.8^{+0.2}_{-1.8}$  times, i.e., only 5000–6000 training images are required for similar accuracy. Finally, we collected distribution samples for 4669 MNIST images from a physical QPU (Quandela Ascella,  $g^{(2)}=1.95\%$ ,  $\mathcal{I}=86.36\%$ ) for QORC (orange circles). We observe performance of  $(26.5^{+3.5}_{-6.0})$  times training size reduction, marginally above the simulations for a perfect photon source but overlapping within error bars. We attribute the slight discrepancy to the sampling nature of our experiments and simulations. This close to ideal performance of the physical QPU is also supported by Fig. 3, where the accuracy of an ideal and real source

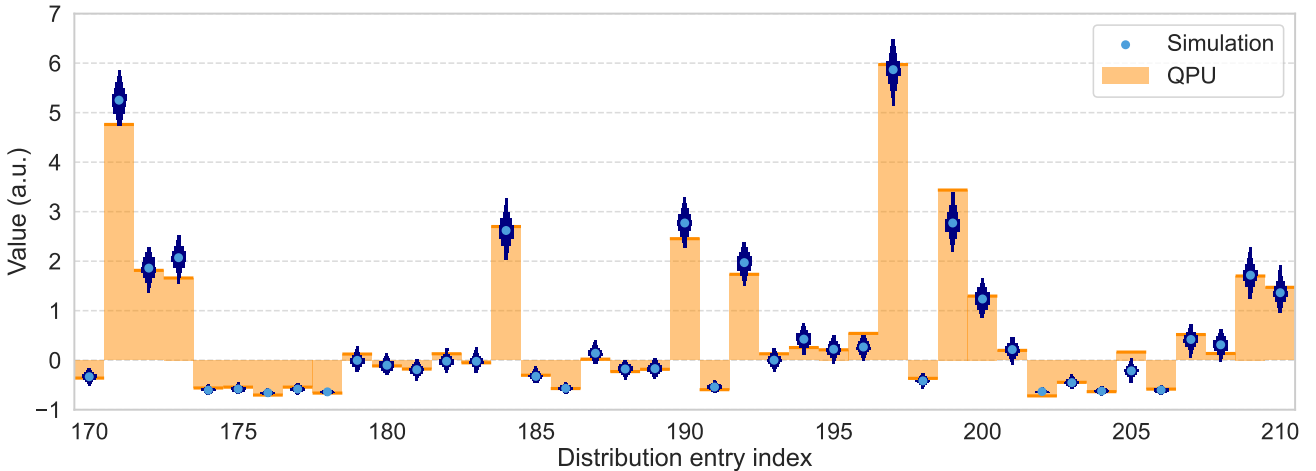


FIG. 6. Comparison of experimental photonic (orange) reservoir distributions with 500 numerical simulations (blue) for the same noise for  $N=3, M=12$  (total of 220 distribution entries). Light blue dots are the means of the 500 numerical simulations, error bars (dark blue) have a thickness proportional to the occurrence of certain values, with top and bottom the minima and maxima. We see a very high overlap between numerical simulations and boson sampling on a quantum cloud platform, qualitatively and quantitatively, even for the moderate 30000 collected samples per image.

(rightmost two brown squares) are close together, and far above the distinguishable photons (leftmost brown square). This QPU-confirmed quantum acceleration has multiple significant implications for real-world applications: 1) lower training costs, computationally and in terms of data labelling efforts; 2) larger independence from data biases; 3) applicability in many domains that naturally have sparse data; and 4) environmental benefits like lower energy consumption and consequently lower carbon footprint.

Finally, we investigate the performance on Quandela's Ascella QPU in more detail, i.e., how closely the distributions from numerical simulations overlap with the photon counting results on the Quandela platform. For a straight comparison, we simulate the experimental values for  $g^{(2)}$  and indistinguishability for the Ascella QPU using three photons into 12 modes. We pick the subset of 4669 images that we processed on the QPU and compare the obtained distributions using different metrics. Firstly, we renormalise the distribution so that the sum equals *one* and all values are positive. In that way, we can use standard distribution comparison metrics and find that they are indeed very similar, with e.g. total variational distance (TVD) =  $0.103 \pm 0.009$  or Jensen-Shannon (JS) divergence =  $0.097 \pm 0.008$ , both ideally *zero* for identical and *one* for maximally different distributions. This is promising, however, not exactly the input into our classifier due to the initial re-normalisation step. Secondly, we use the standardised input distribution for comparison. This distribution is not normalised or strictly positive, it stems from a standardisation to *zero* mean and *unit* variance. Here, we chose the Kolmogorov-Smirnov (KS) statistic and p-value value as a metric because TVD and JS divergence are not applicable. Our value KS =  $0.072 \pm 0.028$  is close to *zero*, which would be the ideal

case for two perfectly overlapping distributions, and the p value =  $0.65 \pm 0.31$  means that the distributions look statistically similar ( $p > 0.05$ ).

Unfortunately, the above numbers alone cannot capture all the nuances of how two distributions differ. E.g., two distributions might have the same KS statistic but differ in shape, skew, or where the differences occur. Plotting the distributions side by side, however, allows the human eye to see these subtleties. Visualisation provides context that a single number might hide, making it easier to understand the practical significance of the differences. Fig. 6 shows such a plot of differences for a subset of distribution entries on one randomly chosen image from MNIST. The photonic experiment on a QPU (orange) is compared to 500 numerical simulations for the same noise (light blue dot is its mean), with the thickness of the error bars corresponding to a histogram of value occurrences. This showcases the high qualitative and quantitative overlap between numerical and photonic experiments, with the obtained *fingerprint* of the image nearly identical within errors. The results from a photonic integrated chip open QORC to all the quantum advantages of boson sampling in terms of scalability, efficiency, and speed.

Following these very encouraging results on the achievable accuracies for different training datasets and significantly lower requirements on the number of training images, we explore the potential of QORC beyond linear classifiers on the MNIST dataset. In order to do this in a fair way, we need to optimise the hyperparameters of the networks under consideration. To find the best architectures for different network models, we employ KerasTuner [43], a scalable hyperparameter optimisation framework within Keras. We compared four models: the L-SVC, a shallow network with a fixed or variable number

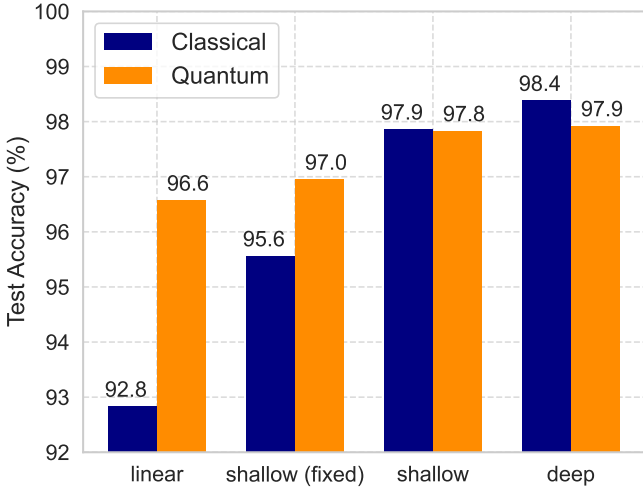


FIG. 7. MNIST classification accuracy for different network architectures. QORC for  $N=3, M=20$ . For each image, the reservoir is 30000 samples. Optimal network parameters found by KerasTuner, iterating 1000 potential models with 30 epochs each. Model search space parameters in Supplementary Material Sec. [S6]. MNIST data with: Blue, no reservoir; Orange, quantum reservoir.

of units, and a deep neural network. We iterate the optimisation over 1000 potential models trained for 30 epochs each and consider the reservoir with  $N=3, M=20$ . Please see the Supplemental Material Sec. [S6] for further details on the procedure and the searched parameter space.

Fig. 7 summarises the results and shows that the improvement of QORC over the non-accelerated neural networks reduces with network complexity. Unexpectedly, adding even a modest-sized reservoir seems to be disadvantageous compared to the original input data for the optimised deep neural network with three hidden layers. We attribute this to an increase in inputs with very noisy or no actual information, i.e., many of the values in the boson sampling distribution are close to zero and prone to undersampling when using a maximal sample size of 30000. This could be avoided by either using a larger number of samples or by identifying more important features in the distribution and feeding only those to the network. Either way, we are not expecting QORC to surpass the performance of a deep neural network as this architecture already offers rich modelling capabilities of non-linear behaviour. We also believe the overall behaviour of reduced improvements by QORC is due to the increased capabilities of the networks to go beyond linear classification. Note that as the network complexity increases, QORC still achieves progressively higher accuracies.

We are currently in a period of exponential improvement in quantum photonics, as the field leverages the capabilities of foundry fabrication [44]. State of the art commercial systems have a transmittance of  $\eta_t \sim 0.22 - 3.04\%$ —which combines circuit throughput and detector

efficiency, but only captures partial aspects of the source efficiency. With typical clock rates of 80MHz, the five-photon rate is  $\eta_{tot} \propto \eta_t^5 \approx 92\text{nHz} - 47\text{mHz}$  [45]. In five years, there will be systems available with 2GHz clock rates and total efficiency of  $\eta_{tot} > 90\%$ , leading to five-photon rates of  $\sim 1.2\text{GHz}$ , an improvement of sixteen to eleven orders-of-magnitude. At that point quantum-accelerated machine learning offers capabilities orders of magnitude greater than those possible with conventional compute.

This work presents a comprehensive analysis of quantum optical reservoir computing, demonstrating its capability for practical and scalable quantum acceleration of classification tasks. QORC consistently outperforms classical linear classifiers across a range of tasks, even for the limits of completely distinguishable photons or a single photon input,  $N=1$ , where only first-order quantum coherence occurs. The scheme achieves comparable or superior test accuracies while requiring up to twenty times fewer training images, highlighting the data-efficiency advantage and acceleration. Crucially, the advantages are experimentally verified on a physical QPU, the Ascella processor by Quandela. The very close quantitative and qualitative agreement between numerical results and experiments on a real quantum photonic processor confirms the physical validity of our reservoir approach. Moreover, QORC shows strong improvements on imbalanced and complex datasets, including artificially imbalanced MNIST and medical images from MedMNISTv2.

Looking forward, future research will be on further expanding QORC’s advantage on physical hardware, focusing on runtime, scalability, and efficiency. Another direction is to advance boson sampling with new techniques that preserve the unique structural fingerprint while reducing the dimensionality of the distribution [46, 47], reducing the inputs to the classifier and hence further accelerating the classification. Extending our framework beyond static image data to e.g. pattern recognition in time-series [48, 49], could reveal new regimes of quantum reservoir performance, particularly for dynamical feature extraction. Ultimately, advancing both the hardware implementation and task diversity of QORC will be key to realising concrete quantum advantage in real-world machine learning tasks.

*Acknowledgements.* We thank Michael Harvey, Jean Senellart, and Sally Shrapnel for valuable discussions. MR is the recipient of a Fellowship funded by the Big Questions Institute; AGW is the recipient of an Australian Research Council Laureate Fellowship (FL210100045) funded by the Australian Government. This research was supported in part by the Australian Research Council Centre of Excellence for Engineered Quantum Systems (EQUS, CE170100009).

\* m.rambach@uq.edu.au

---

[1] H. P. Nautrup, N. Delfosse, V. Dunjko, H. J. Briegel and N. Friis, Optimizing Quantum Error Correction Codes with Reinforcement Learning, *Quantum* **3**, 215 (2019).

[2] S. Khairy, R. Shaydulin, L. Cincio, Y. Alexeev and P. Balaprakash, Learning to Optimize Variational Quantum Circuits to Solve Combinatorial Problems, *Proceedings of the AAAI Conference on Artificial Intelligence* **34**, 2367 (2020).

[3] L. Cheng, Y.-Q. Chen, S.-X. Zhang and S. Zhang, Quantum approximate optimization via learning-based adaptive optimization, *Communications Physics* **7**, 83 (2024).

[4] M. Krenn, M. Malik, R. Fickler, R. Lapkiewicz and A. Zeilinger, Automated Search for new Quantum Experiments, *Physical Review Letters* **116**, 090405 (2016).

[5] A. A. Melnikov, H. Poulsen Nautrup, M. Krenn, V. Dunjko, M. Tiersch et al., Active learning machine learns to create new quantum experiments, *Proceedings of the National Academy of Sciences* **115**, 1221 (2018).

[6] A. Strikis, D. Qin, Y. Chen, S. C. Benjamin and Y. Li, Learning-Based Quantum Error Mitigation, *PRX Quantum* **2**, 040330 (2021).

[7] F. Arute, K. Arya, R. Babbush, D. Bacon, J. C. Bardin et al., Quantum supremacy using a programmable superconducting processor, *Nature* **574**, 505 (2019).

[8] H.-S. Zhong, H. Wang, Y.-H. Deng, M.-C. Chen, L.-C. Peng et al., Quantum computational advantage using photons, *Science* **370**, 1460 (2020).

[9] Y. Wu, W.-S. Bao, S. Cao, F. Chen, M.-C. Chen et al., Strong Quantum Computational Advantage Using a Superconducting Quantum Processor, *Physical Review Letters* **127**, 180501 (2021).

[10] L. S. Madsen, F. Laudenbach, M. F. Askarani, F. Rortais, T. Vincent et al., Quantum computational advantage with a programmable photonic processor, *Nature* **606**, 75 (2022).

[11] H.-L. Liu, H. Su, S.-Q. Gong, Y.-C. Gu, H.-Y. Tang et al., Robust quantum computational advantage with programmable 3050-photon Gaussian boson sampling (2025), arXiv:2508.09092 [quant-ph].

[12] D. A. Abanin, R. Acharya, L. Aghababaie-Beni, G. Aigeldinger, A. Ajoy et al., Observation of constructive interference at the edge of quantum ergodicity, *Nature* **646**, 825 (2025).

[13] S. Aaronson and A. Arkhipov, in *Proceedings of the Forty-Third Annual ACM Symposium on Theory of Computing* (ACM, San Jose California USA, 2011) pp. 333-342.

[14] M. A. Broome, A. Fedrizzi, S. Rahimi-Keshari, J. Dove, S. Aaronson et al., Photonic Boson Sampling in a Tunable Circuit, *Science* **339**, 794 (2013).

[15] A. Crespi, R. Osellame, R. Ramponi, D. J. Brod, E. F. Galvão et al., Integrated multimode interferometers with arbitrary designs for photonic boson sampling, *Nature Photonics* **7**, 545 (2013).

[16] J. B. Spring, B. J. Metcalf, P. C. Humphreys, W. S. Kolthammer, X.-M. Jin et al., Boson Sampling on a Photonic Chip, *Science* **339**, 798 (2013).

[17] M. Tillmann, B. Dakić, R. Heilmann, S. Nolte, A. Szameit et al., Experimental boson sampling, *Nature Photonics* **7**, 540 (2013).

[18] A. Sakurai, A. Hayashi, W. J. Munro and K. Nemoto, Quantum optical reservoir computing powered by boson sampling, *Optica Quantum* **3**, 238 (2025).

[19] S. Nerenberg, O. D. Neill, G. Marcucci and D. Faccio, Photon Number-Resolving Quantum Reservoir Computing (2025), arXiv:2402.06339 [quant-ph].

[20] V. Cimini, M. M. Sohoni, F. Presutti, B. K. Malia, S.-Y. Ma et al., Large-scale quantum reservoir computing using a Gaussian Boson Sampler (2025), arXiv:2505.13695 [quant-ph].

[21] S.-Q. Gong, M.-C. Chen, H.-L. Liu, H. Su, Y.-C. Gu et al., Enhanced Image Recognition Using Gaussian Boson Sampling (2025), arXiv:2506.19707 [quant-ph].

[22] F. Hoch, E. Caruccio, G. Rodari, T. Fracalanci, A. Suprano et al., Quantum machine learning with Adaptive Boson Sampling via post-selection, *Nature Communications* **16**, 10.1038/s41467-025-55877-z (2025).

[23] M. Lukoševičius and H. Jaeger, Reservoir computing approaches to recurrent neural network training, *Computer Science Review* **3**, 127 (2009).

[24] M. Yan, C. Huang, P. Bienstman, P. Tino, W. Lin et al., Emerging opportunities and challenges for the future of reservoir computing, *Nature Communications* **15**, 2056 (2024), publisher: Nature Publishing Group.

[25] R. Martnez-Pea, G. L. Giorgi, J. Nokkala, M. C. Soriano and R. Zambrini, Dynamical Phase Transitions in Quantum Reservoir Computing, *Physical Review Letters* **127**, 100502 (2021).

[26] R. A. Bravo, K. Najafi, X. Gao and S. F. Yelin, Quantum Reservoir Computing Using Arrays of Rydberg Atoms, *PRX Quantum* **3**, 030325 (2022).

[27] P. Pfeffer, F. Heyder and J. Schumacher, Hybrid quantum-classical reservoir computing of thermal convection flow, *Physical Review Research* **4**, 033176 (2022).

[28] Y. Suzuki, Q. Gao, K. C. Pradel, K. Yasuoka and N. Yamamoto, Natural quantum reservoir computing for temporal information processing, *Scientific Reports* **12**, 1353 (2022).

[29] R. Martnez-Pea, J. Nokkala, G. L. Giorgi, R. Zambrini and M. C. Soriano, Information Processing Capacity of Spin-Based Quantum Reservoir Computing Systems, *Cognitive Computation* **15**, 1440 (2023).

[30] A. Suprano, D. Zia, L. Innocenti, S. Lorenzo, V. Cimini et al., Experimental Property Reconstruction in a Photonic Quantum Extreme Learning Machine, *Physical Review Letters* **132**, 160802 (2024).

[31] A. De Lorenzis, M. Casado, M. Estarellas, N. Lo Gullo, T. Lux et al., Harnessing quantum extreme learning machines for image classification, *Physical Review Applied* **23**, 044024 (2025).

[32] A. Sakurai, M. P. Estarellas, W. J. Munro and K. Nemoto, Quantum Extreme Reservoir Computation Utilizing Scale-Free Networks, *Physical Review Applied* **17**, 064044 (2022).

[33] A. Hayashi, A. Sakurai, S. Nishio, W. J. Munro and K. Nemoto, Impact of the form of weighted networks on the quantum extreme reservoir computation, *Physical Review A* **108**, 042609 (2023).

[34] A. D. Lorenzis, M. P. Casado, M. P. Estarellas, N. L. Gullo, T. Lux et al., Harnessing Quantum Extreme Learning Machines for image classification, *Physical Review Applied* **23**, 044024 (2025), arXiv:2409.00998 [quant-ph].

[35] M. Sharifian and A. Bayat, Hybrid Boson Sampling-

Neural Network Architecture for Enhanced Classification (2025), arXiv:2510.13332 [quant-ph].

[36] L. Deng, The MNIST Database of Handwritten Digit Images for Machine Learning Research [Best of the Web], IEEE Signal Processing Magazine **29**, 141 (2012).

[37] F. A. E. Alpaydin, Pen-Based Recognition of Handwritten Digits (1996), uCI Machine Learning Repository at <https://doi.org/10.24432/C5MG6K>.

[38] J. M. Johnson and T. M. Khoshgoftaar, Survey on deep learning with class imbalance, Journal of Big Data **6**, 27 (2019).

[39] J. Yang, R. Shi, D. Wei, Z. Liu, L. Zhao et al., MedMNIST v2 - A large-scale lightweight benchmark for 2D and 3D biomedical image classification, Scientific Data **10**, 41 (2023).

[40] S. S. Haykin, *Neural networks and learning machines*, 3rd ed. (Pearson Education, 2016).

[41] A. Sakurai, A. Hayashi, W. J. Munro and K. Nemoto, Simple hamiltonian dynamics as a powerful resource for image classification, Phys. Rev. A **111**, 052432 (2025).

[42] X. Gao, D. Xie, Y. Zhang, Z. Wang, C. Chen et al., A Comprehensive Survey on Imbalanced Data Learning (2025), arXiv:2502.08960 [cs].

[43] T. O’Malley, E. Bursztein, J. Long, F. Chollet, H. Jin et al., Kerastuner, <https://github.com/keras-team/keras-tuner> (2019).

[44] K. Alexander, A. Benyamin, D. Black, D. Bonneau, S. Burgos et al., A manufacturable platform for photonic quantum computing, Nature **641**, 876 (2025), publisher: Nature Publishing Group.

[45]  $\eta_{tot} = \alpha * RR/N * \eta_t^N * FF * PF$ , with  $N$ , the number of photons,  $\alpha \approx 1/N$  and  $FF * PF = 0.56$ , both factors related to the photon source demultiplexer,  $RR = 80\text{MHz}$ , the repetition rate, and  $\eta_t$ , the transmittance.

[46] B. Seron, L. Novo, A. Arkhipov and N. J. Cerf, Efficient validation of Boson Sampling from binned photon-number distributions, Quantum **8**, 1479 (2024).

[47] M. C. Anguita, A. Camillini, S. Marzban, M. Robbio, B. Seron et al., Experimental validation of boson sampling using detector binning (2025), arXiv:2502.05093 [quant-ph].

[48] K. Kobayashi, K. Fujii and N. Yamamoto, Feedback-driven quantum reservoir computing for time-series analysis, PRX Quantum **5**, 040325 (2024).

[49] E. Jafarigol, B. Alaghband, A. Gilanpour, S. Hosseini poor and M. Mirmozafari, AI/ML-Based Automatic Modulation Recognition: Recent Trends and Future Possibilities (2025), arXiv:2502.05315 [cs].

# Supplemental Material: Photonic Quantum-Accelerated Machine Learning

Markus Rambach,<sup>1,\*</sup> Abhishek Roy,<sup>1,2</sup> Alexei Gilchrist,<sup>2</sup> Akitada Sakurai,<sup>3</sup> William J. Munro,<sup>3</sup> Kae Nemoto,<sup>3</sup> and Andrew G. White<sup>1</sup>

<sup>1</sup>*Quantum Technology Laboratory, School of Mathematics and Physics,  
University of Queensland, Brisbane QLD 4072, Australia*

<sup>2</sup>*Department of Physics and Astronomy, Macquarie University, Sydney NSW 2113, Australia*

<sup>3</sup>*Okinawa Institute of Science and Technology Graduate University, Onna-son, Okinawa 904-0495, Japan*

(Dated: December 10, 2025)

## S1. DIGITS DATA SET

The DIGITS dataset [1] is a classic benchmark in machine learning, consisting of 8-by-8 greyscale images of handwritten digits (09). Each image contains pixel intensity ranging from 0 to 16 in a compact 64-feature representation. The dataset includes 1797 samples, making it lightweight and well-suited for testing algorithms and evaluating classification performance on simple visual tasks and suitable for the current capabilities of a QPU. Compared to datasets like MNIST or MedMNISTv2, DIGITS is smaller and lower resolution, which allows for fast experiments while still capturing key challenges of image recognition like shape variation and noise.

Fig. S1 shows the dependence of the classification accuracy of QORC on the photon indistinguishability for  $N=3, M=12$  (orange) and compares it to the L-SVC (black). The results are noisier than in the MNIST case, with some lower indistinguishabilities performing better than higher ones, however, we believe this is a shot-to-shot effect and will change with other unitaries or a different train/test split. The improvements range from 1.9% to 3.1% for the test accuracies, and 2.8% to 3.2% on training data. The training accuracy is 100% for all indistinguishabilities above 25%.

## S2. CONFUSION MATRIX

A confusion matrix is the visualisation of a table that summarises the performance of a classification model by comparing predicted and true class labels. It shows how often each class is correctly identified (diagonals) and where misclassifications happen (off-diagonals), providing detailed insight beyond overall accuracy. Fig. S2 a), b) illustrates examples of such matrices for the L-SVC and QORC, respectively. They look very similar as the achieved accuracies—defined as the sum of the diagonal over the sum of all values—are above 90% in both cases and differences are subtle. These differences are highlighted individually in Fig. S2 c) which shows a similar confusion matrix representation for QORC b) minus L-SVC a). We clearly see that all values on the diagonal are positive, showing the increase in correctly classified images. Similar, all off-diagonal elements are  $\leq 0$ , showing a

decrease in incorrect classification events. The seemingly larger differences of correct classifications between different classes, e.g., *zero* vs. *one*, mainly stem from slight class imbalances in the test dataset.

## S3. REPRODUCIBILITY

Reproducibility in training classifiers ensures that results can be reliably replicated under the same conditions, which is essential for scientific validity and trust in the model. It allows for the verification of findings, fair comparison of methods, and build upon prior work with confidence. We investigate the differences in accuracies when using different unitaries and/or input states to the boson sampling network ( $N=3, M=12$ ) that creates our quantum data for acceleration. Table S1 lists the mean and standard deviation of the accuracy of QORC with 10 independent runs of boson sampling, all collecting 30000 samples per image. We can see that the results are very

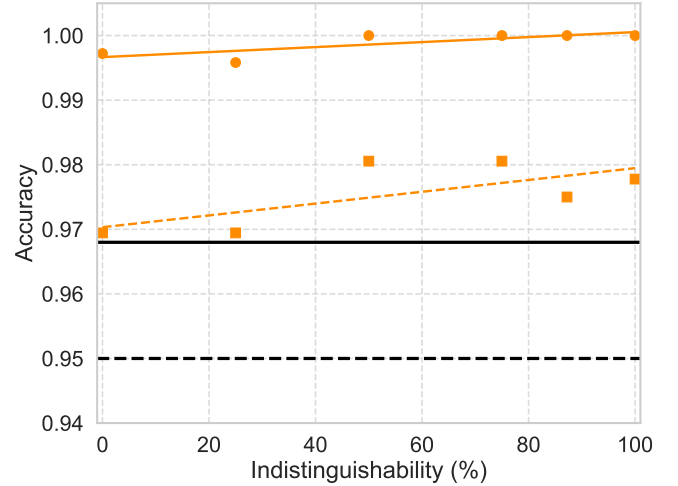


FIG. S1. DIGITS classification accuracy as a function of single photon indistinguishability. QORC with  $N=3, M=12$  in orange, L-SVC in black for comparison. Training as circles and solid lines for 100 epochs, testing as squares and dashed lines. Train/test split is 80/20 (1437/360 images). For each image, the reservoir is 30,000 samples, noise encoded via non-ideal  $g_2$  and indistinguishability. Orange fitted lines to guide the eye only. All accuracies for all indistinguishabilities surpass the maximal achievable training accuracy of L-SVC.

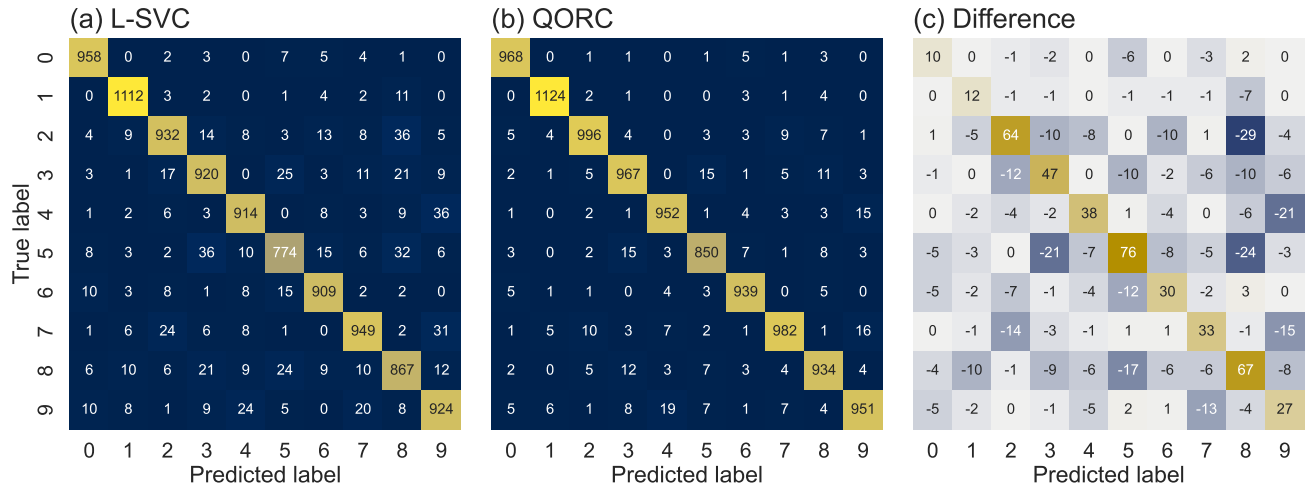


FIG. S2. Confusion matrix examples for MNIST classification on test data, numbers in the matrices indicate classification instances. Training on 60000 images for 100 epochs, testing on 10000 images. Reservoir: 30000 samples. (a) Linear classifier (L-SVC), (b) QORC, (c) Difference: QORC minus L-SVC. Difference is plotted with a different colour map for clarity: shades of gold for positive values, light grey for no difference (values around 0), and shades of dark blue for negative values.

Parameter	Train Accuracy (%)		Test Accuracy (%)	
	Average	STD	Average	STD
Unitary	96.87	0.18	95.62	0.18
Input state	96.81	0.13	95.57	0.13

TABLE S1. MNIST accuracy on Monte Carlo simulations, 100 training epochs. Reservoir: 30000 samples,  $N=3, M=12$ . 10 independent sampling experiments, changing only the value for the *Parameter* column. STD: standard deviation.

similar and independent of the applied random unitary or the selected input channels of the QPU. The standard deviation is small compared to the achieved advantage of QORC over L-SVC and the means lie well within  $1\sigma$ . We are therefore very confident that the majority of values in the main manuscript are very close to their average and will generally only use a single experiment to quantify and show advantages of QORC, unless stated otherwise.

#### S4. INCREASING PHOTON NUMBER

In Table S2 we analyse the dependence of the achievable accuracy on the photon number  $N$  for a fixed number of modes  $M=20$ . Even with just a single photon in the circuit, we see small but measurable improvements over the case of just inputting the 20 PCA components as additional inputs. This reflects that even a single photon can interfere with itself in the circuit, producing a non-linear response that adds new information to the neural network. We also see that the accuracy advantage gets smaller with every additional photon. Note that the boson sampling output space grows combinatorially, so we've increased the number of samples for accurate sampling.

$N$	Added Inputs	Train Acc. (%)	Test Acc. (%)	$\Delta$ L-SVC
1	20	94.2	93.2	0.6
2	190	96.6	95.2	2.6
3	1140	99.5	96.6	4.0
4	4845	100.0	97.4	4.8
5	15504	100.0	97.5	4.9

TABLE S2. MNIST accuracies for different photon inputs. Reservoir:  $N$  photons,  $M=20$  modes, 30000 samples (100k for  $N=4$ , 1M for  $N=5$ ). Training for 100 epochs. Addit. Inputs is the number of additional inputs, i.e., all possible distributions of  $N$  photons into 20 modes.  $\Delta$ L-SVC is the improvement of test accuracy in QORC over L-SVC.

#### S5. IMBALANCED DATASETS

##### Macro F1 score

The macro F1 score is a balanced measure of classifier performance across multiple classes, giving equal weight to each class regardless of its frequency. It is defined as the arithmetic mean of the per-class scores  $F_{1,i}$  defined as

$$F_{1,i} = \frac{2P_iR_i}{P_i + R_i}, \quad (1)$$

where  $P_i$  is the precision and  $R_i$  is the recall of sub-class  $i$ . Precision and recall are defined as

$$P = \frac{TP}{TP + FP}, \quad R = \frac{TP}{TP + FN}, \quad (2)$$

with  $TP$ ,  $FP$ , and  $FN$  the true positive, false positive, and false negative of the confusion matrix.

For example, let's consider the digit 7: a true positive is when the true label and the prediction is 7. A false positive is when the prediction is still 7, but the true label is anything but the prediction. Finally, for a false negative the true label is a 7, but the prediction is any other category. The macro F1 score is then given as

$$F_1^{\text{macro}} = \frac{1}{C} \sum_{i=1}^C F_{1,i}, \quad (3)$$

mitigating all potential imbalances in training and test datasets.

##### Datasets

###### MNIST

Table S4 shows training set weights for differently balanced artificial datasets on MNIST. In the Gaussian case, the majority class in training is *five*. It accounts for 1/5 of the total training images and includes around  $17\times$  more training images than the smallest minority class *zero*. For the severely imbalanced dataset, which was modelled loosely after the medical DermaMNIST dataset below, the majority class is over  $100\times$  more prominent than the smallest minority class, and makes up for  $\sim 2/3$  of all training images. To remove potential biases, we randomly assigned the class weights to actual digits in each run for the severely imbalanced case and investigated 100 different training runs.

Although not as meaningful as the F1 score in the main manuscript, Table S5 shows all the achieved accuracy values on the artificially imbalanced MNIST data sets. We can see that the advantage of QORC increases for larger imbalance; however, the overall test accuracy is significantly lower as expected.

Model	Parameters							
	Hidden Layers	Activation Function	Units per Layer	Dropout Rate	Optimiser	Learning Rate	Batch Size	
Linear	✗	✗	✗	✗	✓	✓	✓	✓
Shallow (fixed)	✗	✓	✗	✓	✓	✓	✓	✓
Shallow	✗	✓	✓	✓	✓	✓	✓	✗
Deep	✓	✓	✓	✓	✓	✓	✓	✗

TABLE S3. Optimisation space for different model architectures. ✓ indicates parameters that are optimised, ✗ parameters that are either not optimised due to time constraints or not applicable (e.g. hidden layers in a linear network).

### MedMNISTv2

Table S6 presents the training set weights for the investigated datasets in MedMNISTv2. Additionally, it highlights the maximally achievable test accuracies with deep neural networks [2], putting the results from Fig. S3 into perspective. We looked at four datasets: OCT (optical coherence tomography images for retinal disease, greyscale), OrganA,S (Axial, Sagittal CT images from liver tumour segmentation, greyscale), and Derma (dermatoscopic images of pigmented skin lesions,

colour). The datasets are diverse with different numbers of training images and classes, standardised via pre-processing and pre-determine train/test splitting, and finally lightweight as 28-by-28(-by-3) pixel images in greyscale (colour). Please see Ref. [2] for further details and metrics.

Fig. S3 illustrates achieved accuracies on MedMNISTv2. We observe that the overall performance of L-SVC and QORC is significantly worse than for imbalanced MNIST, indicating that the algorithms struggle mainly with the higher complexity of the images rather than the imbalanced training data. For comparison, we also added the majority classification, where we just pick the majority class and assign its label to all test images. This leads to almost identical results on accuracy for the L-SVC on the OCT and especially Derma datasets, showing that little is actually being learned by the classical model in both cases. Although the maximally achievable accuracies of deep neural networks are outside the reach of QORC (although not too far away for OrganS

Data	Class Percentages (Numbers 0-9)									
	0	1	2	3	4	5	6	7	8	9
Bal	10	10	10	10	10	10	10	10	10	10
Gauss	1.2	3.5	7.9	13.8	18.8	20.0	16.6	10.7	5.4	2.1
Imbal	64.3	9.7	8.0	6.4	3.9	3.2	1.6	1.3	1.0	0.6

TABLE S4. MNIST imbalance. For ‘‘Gauss’’:  $\mu=4.75$ ,  $\sigma=2$  to keep it centred but slightly asymmetric. For ‘‘Imbal’’: the percentages are randomly shuffled onto the categories in each run. See main text for further details.

Input Data	Modes	Accuracy (%)		
		Train	Test	$\Delta$ L-SVC
Balanced	–	93.6	91.4	–
Balanced	12	98.8	94.4	3.0
Balanced	20	100.0	95.0	3.6
Gaussian	–	95.5	89.1	–
Gaussian	12	99.1	92.4	3.3
Gaussian	20	100.0	93.6	4.5
Severely Imbalanced	–	96.6	84.7	–
Severely Imbalanced	12	99.6	89.0	4.3
Severely Imbalanced	20	100.0	90.0	5.3

TABLE S5. MNIST classification accuracies for differently balanced datasets, QORC for  $N=3$ ,  $M=12/20$ . Training for 100 epochs with  $\sim$ 10000 train images, evaluation on 10000 test images. Top: balanced training data between all categories; Middle: Gaussian filter with  $\mu=4.75$ ,  $\sigma=2$ ; Bottom: Severely imbalanced training data with  $\sim 2 \times (64.3\%)$  images in majority category compared to all other categories.  $\Delta$ L-SVC is the difference to L-SVC.

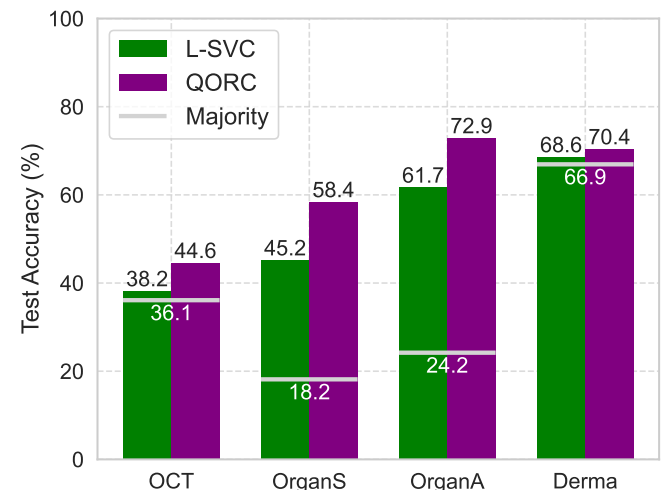


FIG. S3. QORC classification accuracy improvements on different datasets in MedMNISTv2 for 200 training epochs. Quantum reservoir:  $N=3$ ,  $M=20$ ; for each image, the reservoir is 30,000 samples. Majority: classifier which just picks the majority training class each time without learning, value averaged between training and test.

Data	Class Percentages										Acc. (%)	
	OCT	OrganS	OrganA	Derma	OCT	OrganS	OrganA	Derma	OCT	OrganS	OrganA	Derma
OCT	34.4	10.5	8.0	47.2	—	—	—	—	—	—	—	77.6
OrganS	8.2	4.5	4.4	5.2	8.1	8.0	24.9	5.3	5.8	14.4	11.2	81.3
OrganA	5.7	4.0	3.9	4.3	11.5	11.0	17.8	11.3	11.4	8.8	10.3	95.1
Derma	3.3	5.1	11.0	1.1	11.1	67.0	1.4	—	—	—	—	76.8

TABLE S6. MedMNISTv2 class imbalances and maximally achievable test accuracies on deep neural networks according to Ref. [2]. OCT (optical coherence tomography images for retinal disease, greyscale), OrganA,S (Axial, Sagittal CT images from liver tumour segmentation, greyscale), and Derma (dermatoscopic images of pigmented skin lesions, colour)

and Derma), our scheme again outperforms L-SVC in all metrics on all investigated datasets.

## S6. KERASTUNER DETAILS

We compared four different model architectures: L-SVC (Linear), a shallow network with a fixed or variable amount of units (ShallowF and Shallow), and a deep neural network (Deep). All models are trained for 30 epochs to get close to optimal accuracy but finish within reasonable time in training. We optimise over 1000 potential models and investigate the classical and quantum-accelerated cases individually as otherwise KerasTuner favours one case over the other early on and comparison becomes unfeasible. Table S3 presents the optimised parameter space and Table S7 summarises the optimal values found by KerasTuner.

\* m.rambach@uq.edu.au

- [1] F. A. E. Alpaydin, “Pen-Based Recognition of Handwritten Digits,” (1996), uCI Machine Learning Repository at <https://doi.org/10.24432/C5MG6K>.
- [2] J. Yang, R. Shi, D. Wei, Z. Liu, L. Zhao, B. Ke, H. Pfister, and B. Ni, Scientific Data **10**, 41 (2023).
- [3] T. O’Malley, E. Bursztein, J. Long, F. Chollet, H. Jin, L. Invernizzi, *et al.*, “Kerastuner,” <https://github.com/keras-team/keras-tuner> (2019).

Model	Acc.	Parameters							
		Hidden Layers	Activation Function	Units per Layer	Dropout Rate	Optimiser	Learning Rate	Batch Size	
Linear	✗	0	–	–	–	Adam	$6.5 \times 10^{-4}$	256	
	✓	0	–	–	–	Adam	$2.2 \times 10^{-4}$	32	
ShallowF	✗	1	relu	16	0.0	Adam	$3.7 \times 10^{-4}$	32	
	✓	1	relu	16	0.0	Adagrad	$2.0 \times 10^{-2}$	256	
Shallow	✗	1	elu	64	0.0	RMSprop	$2.0 \times 10^{-3}$	–	
	✓	1	relu	96	0.3	RMSprop	$5.0 \times 10^{-4}$	–	
Deep	✗	3	relu	$3 \times 256$	$0.3/0.0/0.1$	Adam	$4.2 \times 10^{-4}$	–	
	✓	3	relu	256/256/32	$0.3/0.4/0.1$	Adam	$2.2 \times 10^{-4}$	–	

TABLE S7. Optimised parameter values for different model architectures: Linear: L-SVC; ShallowF: one hidden layer with fixed number of units (16); Shallow: same as ShallowF but with learnable number of units; Deep: deep neural network with up to 3 hidden layers. Acc.: quantum reservoir accelerated (yes/no, individually investigated); Activation function: relu, elu, tanh; Units per layer: 16 to 256 (9 steps); Dropout rate: 0.0 to 0.5 (6 steps); Optimiser: Adam, Adagrad, RMSprop, SGD; Learning rate:  $10^{-5}$  to  $10^{-1}$  (continuous); Batch size: 32 to 256 (4 steps); See Ref. [3] for further details.